

1 **An empirically constrained forecasting strategy for
2 induced earthquake magnitudes using extreme value
3 theory**

4 James P. Verdon^{1*}, Leo Eisner²

5 *1. School of Earth Sciences, University of Bristol, Wills Memorial Building, Queen's Road,
6 Bristol, United Kingdom.*

7 *2. Seismik s.r.o., Kubišova 1265/8 Praha, Czech Republic.*

8 * Corresponding Author. Email: James.Verdon@bristol.ac.uk, Tel: 0044 117 331 5135.
9 Orcid: 0000-0002-8410-2703

10

11 **Keywords**

12 Induced seismicity; earthquake forecasting

13

14 **Acknowledgements**

15 James Verdon's contribution to this study was funded by the Natural Environment Research Council
16 (NERC) under the SeisGreen Project (Grant No. NE/W009293/1)

17

18 **Declaration of Competing Interests**

19 Both authors have acted and continue to act as independent consultants for a variety of organisations
20 including hydrocarbon operating companies and governmental organisations on issues pertaining to
21 induced seismicity. None of these organisations had any input into the conception, development,
22 analysis or conclusions of this study.

23

24

25

ABSTRACT

27 *Induced seismicity magnitude models seek to forecast upcoming magnitudes of induced earthquakes during the*
28 *operation of subsurface industries such as hydraulic fracturing, geothermal stimulation, wastewater disposal,*
29 *and carbon capture and storage. Accurate forecasting models could guide operational decision-making in real*
30 *time, for example operations could be reduced or paused if forecast models indicate that magnitudes may exceed*
31 *acceptable levels. Robust and transparent testing of forecasting models is required if they are to be adopted by*
32 *operators and regulators of such industries. We develop and test a suite of models based on extreme value*
33 *estimators to forecast the magnitudes of upcoming induced seismic events based on observed seismicity. We*
34 *apply these models to multiple induced seismicity cases from wastewater disposal in Oklahoma and in western*
35 *Texas, as well as other cases of seismicity caused by subsurface fluid injection in North America, Europe, and*
36 *China. In total, our testing dataset consists of more than 80 individual sequences of induced seismicity. We find*
37 *that all the models produce strong correlation between observed and modelled magnitudes, indicating that the*
38 *forecasting provides useful information about upcoming magnitudes. However, some models are found to*
39 *systematically over-predict the observed magnitudes, while others tend to under-predict. As such, the combined*
40 *suite of models can be used to define upper and lower estimators for the expected magnitudes of upcoming events,*
41 *as well as empirically constrained statistical expectations for how these magnitudes will be distributed between*
42 *the upper and lower values. We conclude by demonstrating how our empirically constrained distribution can be*
43 *used to produce probabilistic forecasts of upcoming induced earthquake magnitudes, applying this approach to*
44 *two recent cases of induced seismicity.*

46 1. INTRODUCTION

47 Cases of induced seismicity have grown rapidly over the past two decades, associated with the growth
48 and expansion of oilfield technologies such as hydraulic fracturing, wastewater disposal (WWD), and
49 natural gas storage (NGS). Emerging low-carbon energy technologies such as geothermal and carbon
50 capture and storage, which entail the injection of fluids into the subsurface, also carry the potential to
51 generate induced seismicity.

52 In severe cases, induced seismicity has caused damage to nearby buildings and infrastructure, and
53 injuries to nearby people (e.g., Lee et al., 2019; Lei et al., 2019; Campbell et al., 2020). Even where
54 induced event magnitudes are insufficient to cause damage, they are nevertheless a source of public
55 concern (e.g., Evensen et al., 2022). A failure to adequately manage induced seismicity during
56 development of subsurface geo-energy projects has led to the cancellation of individual projects and
57 sites, and limits or even moratoria being imposed on entire industries. The need to develop methods to
58 quantify induced seismicity hazard during operations, primarily by estimating what magnitudes of
59 earthquakes are likely to be generated, is clear.

60 Our aim in this study is to forecast the growth in earthquake magnitudes as induced seismicity
61 sequences develop. We do this by tracking the magnitudes of new record-breaking events – events that
62 are larger than any previous event within a sequence. We refer to these record-breaking magnitudes as
63 M_{NRB} hereafter. The growth of record-breaking events is of particular importance to operators and
64 regulators of subsurface industries, since their magnitudes will usually determine the largest ground
65 motions that are generated, and therefore the largest impact to nearby buildings, infrastructure, and
66 people. If we are able to accurately forecast upcoming record-breaking magnitudes (and preferably, a
67 probability distribution thereof), this could enable operators to make decisions to ensure the safety of
68 their activities by, for example, reducing, ceasing, or applying other mitigation actions to their
69 operations if it becomes likely that unacceptably high magnitudes will be generated.

70 71 1.1. Observed versus physically possible induced seismicity magnitudes

72 The largest record-breaking event within an induced seismicity sequence is, by definition, the largest
73 event within that sequence. The largest observed magnitude during a sequence of induced seismicity
74 (or a forecast thereof) is commonly referred to as M_{MAX} (e.g., Hallo et al., 2014; van der Elst et al.,
75 2016; Eaton and Igonin, 2018; Verdon and Bommer, 2021). This is different from the M_{MAX} parameter
76 used in tectonic seismic hazard assessment, where it denotes the largest magnitude earthquake that is
77 physically possible given the particular tectonic circumstances in question (e.g., Mueller, 2010). The
78 largest possible magnitude represents a truncation to the Gutenberg and Richter (1944) magnitude-
79 frequency distribution (G-R hereafter). We refer to this truncation magnitude as M^T_{MAX} to differentiate
80 these terms.

81 In making this distinction, we recognise that there is a fundamental difference between tectonic and
82 induced seismicity (Bommer, 2022). Tectonic seismicity is driven by processes acting over geological
83 timescales. Theoretically, all tectonic earthquake populations will eventually be truncated at M^T_{MAX} if
84 we are only able to wait for long enough observation times. In contrast, induced seismicity is driven
85 by a human-induced perturbation that is of limited spatial extent and temporal duration. We are
86 therefore able to observe induced sequences in their entirety, from start to finish. The largest induced
87 event that actually occurs (M_{MAX}) will probably not correspond to the largest possible event at which
88 the G-R distribution would truncate (M^T_{MAX}) unless a sufficient number of induced events have been
89 generated (Zöller and Holschneider, 2016; van der Elst et al., 2016; Eaton and Igonin, 2018).

90 There are some cases of induced seismicity, usually in settings with fairly specific and unique
91 geomechanical conditions, where truncations of the G-R distribution have been observed (e.g., Verdon

92 et al., 2018). However, for most sequences of induced seismicity there has been little robust evidence
93 of truncations to the G-R distribution at high magnitudes, as would be observed if M^T_{MAX} were regularly
94 being reached (e.g., van der Elst et al., 2016; Watkins et al., 2023). It is therefore reasonable in most
95 cases to treat the magnitudes of an ongoing induced seismicity sequence as being drawn from an
96 unbounded G-R distribution unless specific evidence to the contrary is available.

97 Furthermore, the accumulation of tectonic strain that drives tectonic earthquakes is assumed to be
98 relatively constant (with respect to the timescales of our observations). In contrast, the human-made
99 perturbations that drive induced seismicity may quickly increase in scale and spatial extent during
100 operations, for example as injection continues in a given well. As a result, induced seismicity
101 sequences may be expected to grow as injection progresses.

102 While van der Elst et al. (2016) suggested that the order in which induced earthquakes occur is random,
103 subsequent analyses of induced seismicity sequences have shown evidence for progression of event
104 magnitudes as sequences have grown (e.g., Skoumal et al., 2018; Verdon and Bommer, 2021; Watkins
105 et al., 2023). Whereas estimates of the maximum possible magnitude, M^T_{MAX} , should be constant, as
106 this parameter is controlled by underlying physical conditions (e.g., the size and frictional properties
107 of nearby faults), forecasts of M_{MAX} during induced seismicity may be time-dependent, since we should
108 expect a different maximum magnitude event to occur if, for example, we were to inject a given volume
109 of fluid for only 1 month, versus injecting the same volume of fluid every month for a period of years.

111 **1.2. Forecasting induced seismicity magnitudes**

112 A range of methods to forecast magnitudes during induced seismicity sequences have been developed.
113 One approach is to use numerical geomechanical simulations of subsurface processes (e.g., Rutqvist
114 et al., 2013; Verdon et al., 2015; Dempsey and Suckale, 2017). However, such modelling is often
115 difficult to apply in practice since a detailed characterisation of the subsurface is required to generate
116 a model. For many cases, the causative faults on which induced seismicity occurred were not visible
117 in geophysical surveys acquired prior to the onset of industrial activities (e.g., Eaton et al., 2018; Cesca
118 et al., 2021; Nantanoi et al., 2022). Even where faults are successfully imaged, quantification of their
119 mechanical and frictional properties, as required for accurate numerical geomechanical modelling, can
120 be challenging.

121 The alternative to physics-based numerical modelling is to use statistics-based approaches. For these
122 methods the observed population of seismic events is characterised statistically, and the statistical
123 models are then used to make forecasts of the ongoing seismicity. A commonly used approach is to
124 characterise a relationship between the rate of seismicity and the volume of fluids injected into (or
125 removed from) the subsurface at an early stage of operations (e.g., McGarr, 1976, Shapiro et al., 2010;
126 Hallo et al., 2014; Mancini et al., 2021). The future seismicity can then be forecast by extrapolating
127 this relationship to a future planned injection (or production) volume. This approach has been used to
128 forecast seismicity and guide decision-making for several notable cases of induced seismicity,
129 including the Helsinki St1 Deep Heat project (Kwiatek et al., 2019), the Weyburn Carbon Capture and
130 Storage Project (Verdon, 2016), and during hydraulic fracturing of the Preston New Road shale gas
131 wells in Lancashire, UK (Clarke et al., 2019; Kettleby et al., 2021). Verdon et al. (2024) published a
132 comprehensive appraisal of the performance of the Shapiro et al. (2010) and Hallo et al. (2014) models
133 across a wide range of WWD-induced seismicity case studies.

134 135 **1.3. Forecasting induced seismicity magnitudes using extreme value estimators**

136 An alternative approach relies solely on the characterisation of the earthquake population, without any
137 reference to injection or production rates or any other subsurface information. This approach, applied

138 by Mendecki (2016) for mining induced seismicity, is based on the theory of extreme value estimators
 139 developed by Cooke (1979) and is related to methods developed to estimate tectonic M_{MAX}^T values
 140 from observed natural earthquake populations (e.g., Kijko, 2004). The relative simplicity of this
 141 method, since it does not require any operational or geological information, is an attractive aspect of
 142 this approach. A limitation is the need for a catalog of observed seismicity to make a forecast.
 143 However, for cases of induced seismicity we are often able to observe the seismicity to a low
 144 magnitude of completeness if dedicated monitoring systems are installed before the start of operations.

145 Mendecki (2016) applied two approaches to forecasting induced seismicity magnitudes using the order
 146 statistics theory of Cooke (1979). For a random sample of n magnitude observations, M^O , drawn from
 147 a constant underlying distribution, the upper limit for future such observations can be estimated as:

$$M_{UL} = 2M_n^O - \sum_{i=1}^{n-1} \left[\left(1 - \frac{i}{n}\right)^n - \left(1 - \frac{i+1}{n}\right)^n \right] M_{n-i}^O \quad (1)$$

148 where M_i^O represents the event magnitudes sorted into size order, from smallest to largest, such that
 149 M_n^O is the largest event observed to date, which we refer to as M_{MAX}^O .

150 Alternatively, one can consider the jumps in magnitude between events, ΔM^O , since an estimate for
 151 the next largest event can be obtained by adding the estimated maximum jump, ΔM_{MAX} , to the observed
 152 largest event. We refer to this estimate as the “jump-limited” magnitude:

$$M_{JL} = M_{MAX}^O + \Delta M_{MAX} \quad (2)$$

153 The maximum jump is calculated using the same formulation as Equation 1, but applied to the
 154 distribution of magnitude jumps:

$$\Delta M_{MAX} = 2\Delta M_{n_j}^O - \sum_{i=1}^{n_j-1} \left[\left(1 - \frac{i}{n_j}\right)^{n_j} - \left(1 - \frac{i+1}{n_j}\right)^{n_j} \right] \Delta M_{n_j-i}^O \quad (3)$$

155 where ΔM_i^O represents the magnitude jumps ordered from smallest to largest, and n_j is the number of
 156 jumps. There are several ways in which these methods can be applied in practice to forecast induced
 157 event magnitudes (see Section 2 for further details). For example, since these estimators can be applied
 158 to any quantity, the input to these equations can be magnitudes, seismic moments, or potencies.

159 Our aim in this study is to forecast the magnitudes of new record-breaking events during induced
 160 seismicity sequences (M_{NRB}). The two magnitude estimators defined above, M_{UL} and M_{JL} , provide a
 161 means by which this can be done. We might normally expect M_{NRB} values to follow the jump-limited
 162 estimator, since this explicitly describes the jumps to new record-breaking magnitudes. However, there
 163 is a possibility that the next event to occur is at (or close to) the upper limit value as given by the M_{UL}
 164 estimator. We therefore might expect to find, in practice, a distribution of M_{NRB} observations, with
 165 most cases falling close to the M_{JL} values, but with some events falling closer to the M_{UL} estimate.
 166 Hence, our approach is to combine our estimates of M_{UL} and M_{JL} to produce a combined estimator for
 167 M_{NRB} .

168 We note that in forecasting record-breaking events, the implicit assumption is that induced event
 169 magnitudes will continue to grow during a sequence. In reality, induced seismicity sequences may
 170 stabilise and decrease, either as pressures stabilise in large, open reservoirs (e.g., Verdon et al., 2024),
 171 or in response to successful mitigating actions taken by operators. Clearly, forecasting methods that
 172 include an implicit assumption that new record-breaking magnitudes will occur may not be appropriate
 173 in such circumstances. In Section 5.3 we discuss how it might be possible to identify when an induced
 174 seismicity sequence is decaying such that forecasting new record-breaking events is no longer
 175 appropriate. Likewise, the methods presented in Equations 1 – 3 do not provide any temporal

176 constraint – when might a new record-breaking event be expected to occur? Again, in Section 5.3 we
177 provide some discussion as to how temporal constraints could be introduced.

178

179 **1.4. The need for performance assessment of induced seismicity forecasting models**

180 If induced seismicity forecasting models are to be used to guide decision-making at active industrial
181 sites, then there is a clear need for robust, transparent testing of such models. Only through robust
182 testing can we gain confidence in the performance of models such that they can be relied on to guide
183 operational decisions that, on the one hand, may compromise significant financial investments (if
184 projects are abandoned due to potential induced seismicity hazard), while on the other hand could
185 compromise public safety (if larger magnitude events are allowed to occur without mitigation). The
186 public often takes a strong interest in the occurrence of induced seismicity, and so model testing must
187 be transparent and reproducible as a loss of trust of public in ability to safely conduct underground
188 energy operations easily results in loss of social license to operate and rejection of future projects.

189 Empirical testing of forecasting models can go beyond simple assessments of performance since results
190 can be used to feed back into future forecasts. In our case, we anticipate that record-breaking
191 magnitudes will follow the M_{JL} estimator but we allow for the possibility that magnitudes could jump
192 to the upper limit M_{UL} value. As such, the M_{JL} and M_{UL} values may provide lower and upper estimates
193 for M_{NRB} , respectively. A suite of models could be combined to produce an overall estimate (and
194 preferably, a probability distribution thereof) for upcoming induced event magnitudes. An overall
195 estimate from a suite of models should consider the observed performances of the different modelling
196 strategies as applied to large numbers of induced seismicity case studies.

197

198 **1.5. Study objectives**

199 The objective of this study is to provide a systematic assessment of the performance of the M_{UL} and
200 M_{JL} estimators as applied to a large number of cases of injection-induced seismicity. We evaluate
201 several different ways in which these methods can be applied, for example using earthquake
202 magnitudes versus potencies as the inputs to Equations 1 – 3; and using all observed events and jumps
203 as inputs versus only the events and jumps that represent new record-breaking events (see Section 2).
204 In doing so, we investigate the influence of these different formulations on the resulting M_{NRB} forecasts
205 and quantitatively compare their respective performances.

206 Our observations across a large number of induced seismicity sequences provide empirical data on the
207 behaviour of record-breaking magnitudes relative to the M_{UL} and M_{JL} estimators. These observations
208 allow us to define an empirically constrained estimator for M_{NRB} , where the next record-breaking
209 magnitude is expected to fall within a statistical distribution that is defined based on the M_{UL} and M_{JL}
210 estimates.

211 **2. METHODS**

212 Equations 1 – 3 describe two approaches to estimating induced event magnitudes. M_{UL} describes the
213 expected upper limit magnitude based on the population of observed events to date. M_{JL} defines the
214 expected next record-breaking magnitude based on the population of magnitude jumps, with the largest
215 expected magnitude jump being added to the largest observed event to date.

216 For both of these estimates, calculations can use either the earthquake magnitudes or seismic moments,
217 M_0 (or potencies, $P = M_0/G$, where G is the shear modulus). Hereafter, we refer to results computed
218 using magnitudes with the subscript MM , and results computed using potencies with the subscript MO .
219 Furthermore, the magnitudes and magnitude jumps used as inputs to Equations 1 – 3 can be taken from

220 the entire event catalog, where M^0_i represents the entire event population sorted into size order and
 221 ΔM^0_i represents the magnitude (or potency) jump between every event when the entire population is
 222 sorted into magnitude order, with ΔM^0_i then being sorted into size order. Alternatively, one can use an
 223 event population that consists only of the record-breaking events as they appear in a sequence, where
 224 M^0_i represents the record-breaking events sorted into size order, and ΔM^0_i represents the jumps
 225 between the record-breaking events. Hereafter, we refer to calculations using the entire event
 226 population resorted into size order with the subscript $_{AE}$ (for all events) and calculations using only the
 227 record-breaking events as $_{RB}$ (for record-breaking events). These combinations mean that we have a
 228 total of 8 possible ways in which induced event magnitudes can be estimated. These are summarised
 229 in Table 1.

230 *Table 1: Summary of different model implementations used for M_{NRB} forecasting*

Model No.	Model Name	Upper Limit [UL] or Jump-Limited [JL] formula	All Events in Size Order [AE] or Record Breaking only [RB]	Magnitudes [MM] or Potencies [MO]
1	$M_{UL, RB, MM}$	UL	RB	MM
2	$M_{UL, RB, MO}$	UL	RB	MO
3	$M_{UL, AE, MM}$	UL	AE	MM
4	$M_{UL, AE, MO}$	UL	AE	MO
5	$M_{JL, RB, MM}$	JL	RB	MM
6	$M_{JL, RB, MO}$	JL	RB	MO
7	$M_{JL, AE, MM}$	JL	AE	MM
8	$M_{JL, AE, MO}$	JL	AE	MO

231
 232 We note that dedicated microseismic monitoring arrays often produce large numbers of events (e.g.,
 233 Verdon and Budge, 2018), but even for a very large catalog ranging across several orders of magnitude
 234 we often observe only a few record-breaking events. Thus, the methods based on record-breaking
 235 versus all events represent different approaches to statistical estimates. By definition, the record-
 236 breaking method excludes aftershocks as these are smaller than, and occur after, a mainshock and
 237 therefore do not contribute to record-breaking series. However, the approach based on all events
 238 includes aftershocks in the evaluation of the maximum magnitude while representing whole sequence.

239 Given the different ways in which these estimators can be applied to induced seismicity sequences,
 240 there is a clear need to produce a quantitative comparison of their relative performance in forecasting
 241 magnitudes during induced seismicity sequences. Several studies have applied various versions of the
 242 M_{UL} and/or M_{JL} methods to cases of induced seismicity (Cao et al., 2020; Verdon and Bommer, 2021;
 243 Watkins et al., 2023; Schultz et al., 2023a; Cao et al., 2024). In general, these studies have produced
 244 results that show that, at least from a qualitative perspective, these methods do provide useful
 245 forecasting potential. Whereas Mendecki (2016) formulated these methods in terms of seismic
 246 potency, all of the later studies have used earthquake magnitudes. Cao et al. (2020) applied the M_{UL}
 247 and M_{JL} methods to the seismicity induced by gas production at Groningen and to a case of hydraulic
 248 fracturing-induced seismicity in North America. In their calculations, they used all events and jumps
 249 within the catalogs, not just record-breaking ones.

250 Verdon and Bommer (2021) applied the M_{JL} approach to a compilation of 22 instances of hydraulic
 251 fracturing-induced seismicity, and Watkins et al. (2023) applied the M_{JL} approach to 27 cases of
 252 seismicity induced by WWD and NGS. Like Cao et al. (2020), Verdon and Bommer (2021) and
 253 Watkins et al. (2023) used the jumps between all events (when sorted into size order), not just the
 254 jumps to new record-breaking events.

255 Cao et al. (2024) applied the M_{JL} approach to 15 cases of induced seismicity (mostly consisting of the
 256 same hydraulic fracturing sequences examined by Verdon and Bommer, 2021), but using as input to
 257 their model only the population of jumps that created new record-breaking events. Schultz et al.
 258 (2023a) applied the M_{JL} approach to the sequence of WWD-induced seismicity at Musreau Lake,

259 Alberta. Like Cao et al. (2024), they used as inputs only the population of jumps that created new
260 record-breaking events.

261 For all the above studies, the assessment of model performance has been somewhat unsystematic.
262 Mendecki (2016) demonstrated his methods by application to a single example of mining-induced
263 seismicity but did not make any quantitative assessment of model performance. Likewise, Cao et al.
264 (2020) and Schultz et al. (2023a) simply compared the evolution of the observed earthquakes with the
265 changing M_{NRB} estimates, noting that the models generally did a reasonable job of fitting the observed
266 magnitudes. Verdon and Bommer (2021) and Watkins et al. (2023) produced cross-plots of modelled
267 versus observed M_{MAX} (the largest magnitude within each sequence), while Cao et al. (2024) compared
268 modelled and observed magnitudes each time a new record-breaking event occurred (M_{NRB}). These
269 plots showed evidence for correlation between observed and modelled magnitudes, but also showed
270 that at times the M_{JL} model can underestimate M_{NRB} . As such, there has not yet been any effort to
271 systematically quantify the performance of these methods, either between the different methods, or for
272 the same method between different sites. In the following section we introduce the datasets that we
273 use to assess the performance of each method, before presenting our results in Section 4.

274 **3. DATASETS**

275 **3.1. Oklahoma and southern Kansas**

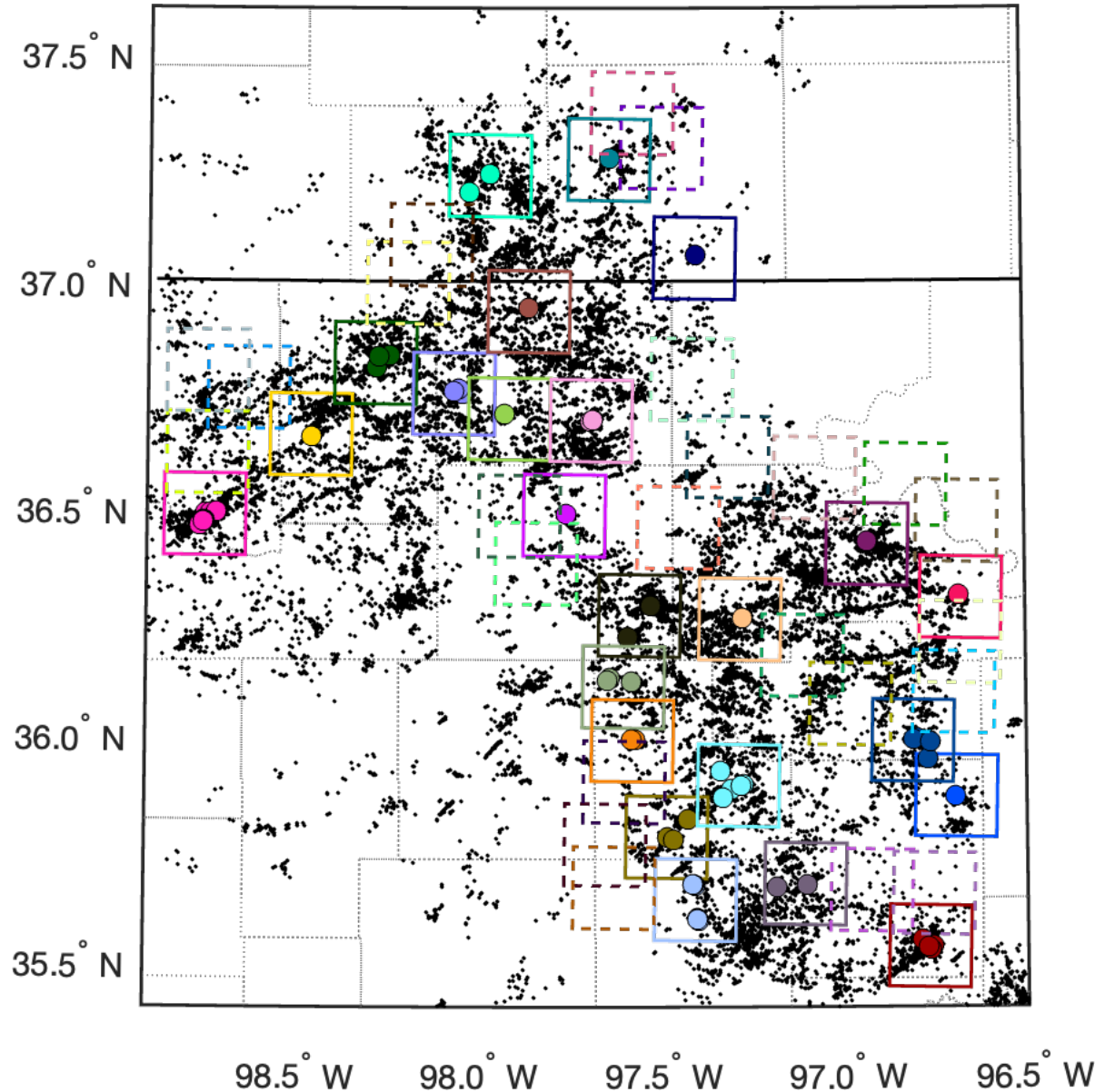
276 WWD in central and northern Oklahoma and southern Kansas (OK-KS hereafter) has increased
277 significantly over the past two decades, driven primarily by a move towards hydrocarbon production
278 from reservoirs with high water fractions, with the produced water then requiring disposal (Rubenstein
279 and Mahani 2015). WWD, primarily into the deep Arbuckle Formation, has caused significant amounts
280 of induced seismicity (Weingarten et al. 2015), including some of the largest induced events to have
281 ever been recorded from fluid injection activities, such as the M 5.6 Prague (Keranen et al., 2013) and
282 M 5.8 Pawnee (Yeck et al., 2017) sequences. Induced seismicity in Oklahoma has also been caused
283 by hydraulic fracturing (e.g., Holland, 2013; Skoumal et al., 2018; Verdon and Rodríguez-Pradilla,
284 2023), particularly in the Anadarko Basin. However, our focus here is on central and northern
285 Oklahoma and southern Kansas, where the bulk of the seismicity is caused by WWD.

286 In this study we use the earthquake catalog published by Park et al. (2022), who used the PhaseNet
287 deep learning model (Zhu and Beroza, 2019) to detect earthquakes recorded by publicly available
288 seismic networks in the OK-KS region. The deep learning model produced a significant increase in
289 event detection, improving detection thresholds by at least 1 magnitude unit over pre-existing
290 earthquake catalogs for the region. We adopt a minimum magnitude of completeness of $M_C = 1.5$,
291 based on the magnitude-frequency relationships plotted in Figure 2 of Park et al. (2022). To estimate
292 potencies from the given magnitudes, we adopt a single value of $G = 20$ GPa (this value is adopted for
293 all sequences in our study).

294 There are 70 earthquakes in the Park et al. (2022) catalog with magnitudes ≥ 4.0 . Some of these events
295 occur in close spatial proximity to each other such that they can be considered to be part of the same
296 sequence. Park et al. (2022) identified clear, discrete fault structures that were responsible for hosting
297 most of the larger magnitude events. These structures typically had lengths of between 5 – 20 km (see
298 Figures 1 and 2 of Park et al., 2022). Where multiple $M \geq 4.0$ events were located within 10 km of
299 each other, we treated these as being part of the same sequence of induced events. In doing so, we
300 identified 24 individual sequences in which induced event magnitudes reached or exceeded $M 4.0$ (see
301 Figure 1). We take these 24 sequences as test datasets for our analysis. For each case, we define a
302 20×20 km square around the $M \geq 4.0$ event (or the largest event for sequences which contain more
303 than one $M \geq 4.0$ event). All earthquakes within this square are taken as representing part of the
304 sequence and used to perform our M_{MAX} forecasting. The $M \geq 4.0$ events, and the 20×20 km squares

305 around them, are shown in Figure 1. The choice of dimensions (20×20 km) was somewhat arbitrary,
306 but we found that such dimensions were usually sufficient to capture the bulk of the seismic events
307 that occurred on each of the discrete fault strands that hosted larger events, as identified by Park et al.
308 (2022).

309



310

311 *Figure 1: Map of the OK-KS study area. Black dots show all earthquakes with $M \geq 1.5$ and coloured*
312 *circles show events with $M \geq 4.0$. The solid boxes show the 20×20 km blocks around each of the*
313 *sequences containing $M \geq 4.0$ events, while the dashed boxes show 20×20 km blocks in which 500*
314 *events were recorded with no $M \geq 3.5$ events. The box colours used in this figure correspond to the*
315 *marker colours used in Figure 3.*

316

317 In testing induced seismicity forecasting models, there can be a tendency to focus on cases where
318 larger magnitude events occurred, since these cases tend to attract the most attention (from the public
319 and policy makers, as well as from academics). However, comprehensive testing should include
320 sequences that did not reach larger magnitudes, since our objective is to develop models that can

321 differentiate between sequences that do, and that do not, escalate to higher magnitude events. Hence,
322 in addition to the 24 sequences with $M \geq 4.0$ events, we identify the same number of cases where
323 magnitudes did not exceed $M 3.5$, selecting twenty-four 20×20 km blocks at random within the study
324 area that contained at least 500 events but no events with $M \geq 3.5$. To do so, we randomly generated
325 block positions and rejected those that did not meet these criteria, continuing until we had 24 cases.
326 The 24 blocks without larger magnitude events are also shown in Figure 1.

327 There is some overlap between the different blocks that are treated hereafter as discrete induced
328 seismicity sequences, meaning that some events are included in more than one forecast. This will create
329 some partial dependence between results from individual sequences. However, in our view a smaller
330 event that is mid-way between the future locations of two different larger events could be reasonably
331 considered to be a precursor to either or both, and so it is reasonable that such events could be included
332 within the forecasts for both larger events, and this partial dependence cannot therefore be avoided.

334 **3.2. Permian Basin, western Texas**

335 Induced seismicity has been recognised in the Permian Basin of western Texas (WTX hereafter) since
336 the 1970s (Davis and Pennington, 1989). Rates of seismicity in the basin have increased substantially
337 since 2015 (Skoumal et al., 2020), associated with WWD and hydraulic fracturing. Given the co-
338 location of these activities, distinguishing causality between WWD and hydraulic fracturing can be
339 challenging, although the bulk of the seismicity is thought to have been caused by WWD (Grigoratos
340 et al., 2022). Three $M \geq 5.0$ events have been induced in this basin: the March 2020 $M 5.0$ event near
341 to the city of Pecos in Reeves County (Skoumal et al., 2021), the November 2022 Coalson Draw $M 5.4$
342 event in western Reeves County, and the December 2022 $M 5.2$ event in Martin County, just to the
343 north of the city of Midland (Hennings and Young, 2023).

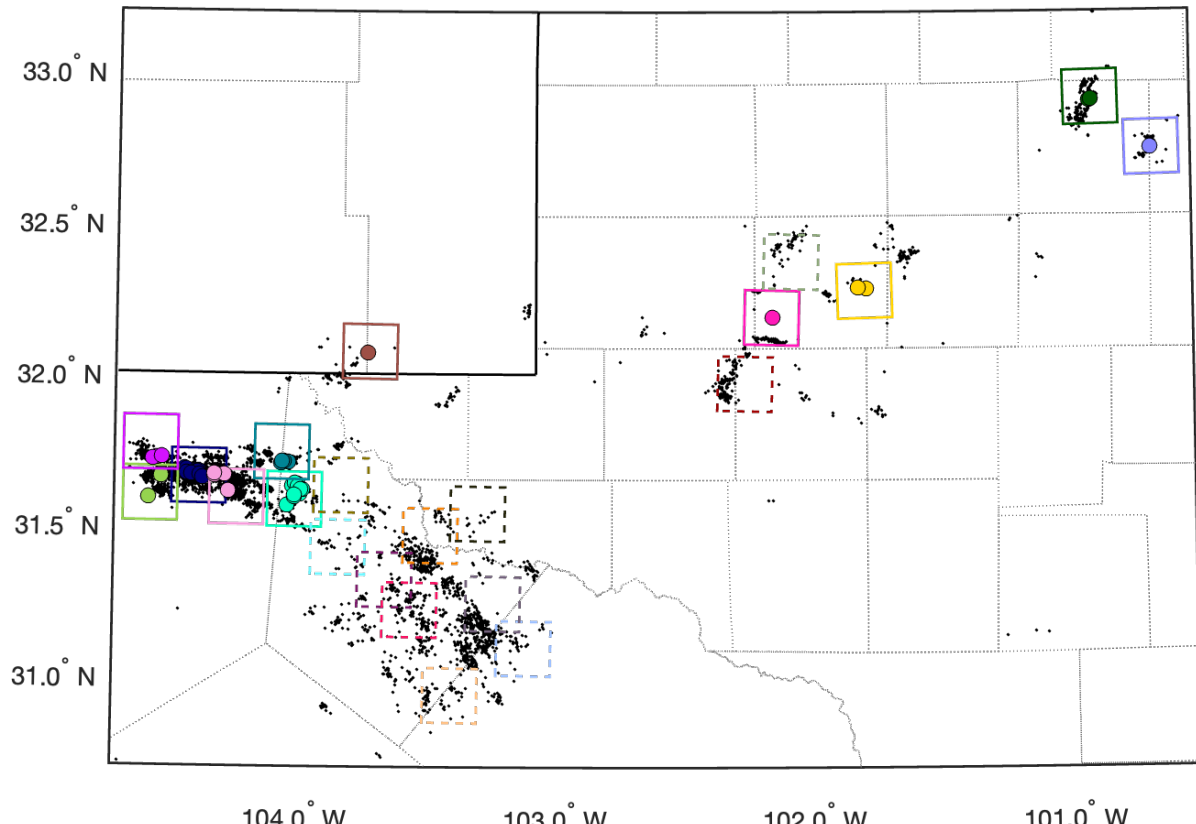
344 In this study we use the TexNet earthquake catalog (Savvaidis et al., 2019), with data running from
345 the start of 2017 until April 2023. We computed the minimum magnitude of completeness by
346 evaluating the lowest magnitude at which the cumulative magnitude-frequency distribution was
347 consistent with the G-R distribution, as assessed by the Kolmogorov-Smirnov test with an acceptance
348 criterion of 10 % (Clauset et al., 2009), which gave $M_C = 2.0$. There are 48 events for which $M \geq 4.0$
349 (Figure 2). Our examination of the temporal and spatial evolution of the seismicity identified 11
350 individual sequences in which induced event magnitudes reached or exceeded $M 4.0$. Much like for
351 our OK-KS datasets, we define 20×20 km squares around each sequence and use all events within
352 these blocks to perform our M_{NRB} forecasting. We then identify an equal number (i.e., 11) of 20×20
353 km blocks containing at least 100 events (we use a lower criterion here recognising the lower number
354 of events in the TexNet catalog compared to the Park et al. (2022) catalog for OK-KS) but no events
355 larger than $M 3.5$, in order to test M_{NRB} model performance for cases where larger magnitude events
356 did not occur.

357 358 **3.3. Watkins et al. (2023) sequences**

359 Watkins et al. (2023) published M_{MAX} forecasts using the $M_{JL_SO_MM}$ formulation for more than 20
360 individual sequences of WWD and NGS-induced seismicity. Some of the Watkins et al. (2023)
361 sequences are already included in our OK-KS and WTX datasets described in the previous sections
362 (Reeves and Cogdell in Texas, Cushing, Fairview, Guthrie-Langston, Pawnee and Prague in
363 Oklahoma, Milan and Harper in Kansas), while for some older sequences with lower levels of
364 monitoring, the largest events occurred before a sufficient number of events were available to compute
365 M_{NRB} estimates (e.g., the Cordel sequence in Alberta). This left 16 additional sequences which we were
366 able to include in our analysis, including: the Azle-Reno, Dallas-Fort Worth, Venus, Timpson and

367 Irving sequences in eastern Texas (Hennings et al., 2021; Frohlich et al., 2014); the Guy-Greenbrier
 368 sequence in Arkansas (Horton, 2012); the Youngstown sequence in Ohio (Kim, 2013); the Paradox
 369 Valley, Greeley and Raton Basin sequences in Colorado (Block et al., 2014; Yeck et al., 2016; Nakai
 370 et al., 2017); the Eagle West, Graham, and Musreau Lakes sequences in western Canada (Horner et
 371 al., 1994; Hosseini and Eaton, 2018; Li et al., 2022); the Rongchang sequence in the Sichuan Basin
 372 (Wang et al., 2020); the Castor project in the Gulf of Valencia, Spain (Cesca et al., 2021); and the
 373 Puerto Gaitán sequence, Colombia (Molina et al., 2020). For each of these sequences, we use the
 374 earthquake catalogs published in the Supplementary Materials of Watkins et al. (2023). We refer to
 375 these sequences as the W23 cases hereafter.

376



377

104.0° W 103.0° W 102.0° W 101.0° W

378

379 *Figure 2: Map of the western Texas study area. Black dots show all earthquakes with $M \geq 1.0$ and*
 380 *coloured circles show events with $M \geq 4.0$. The solid boxes show the 20×20 km blocks around each*
 381 *of the sequences containing $M \geq 4.0$ events, while the dashed boxes show 20×20 km blocks in which*
 382 *100 events were recorded with no $M \geq 3.5$ events. The box colours used in this figure correspond to*
 383 *the marker colours used in Figure 4.*

384

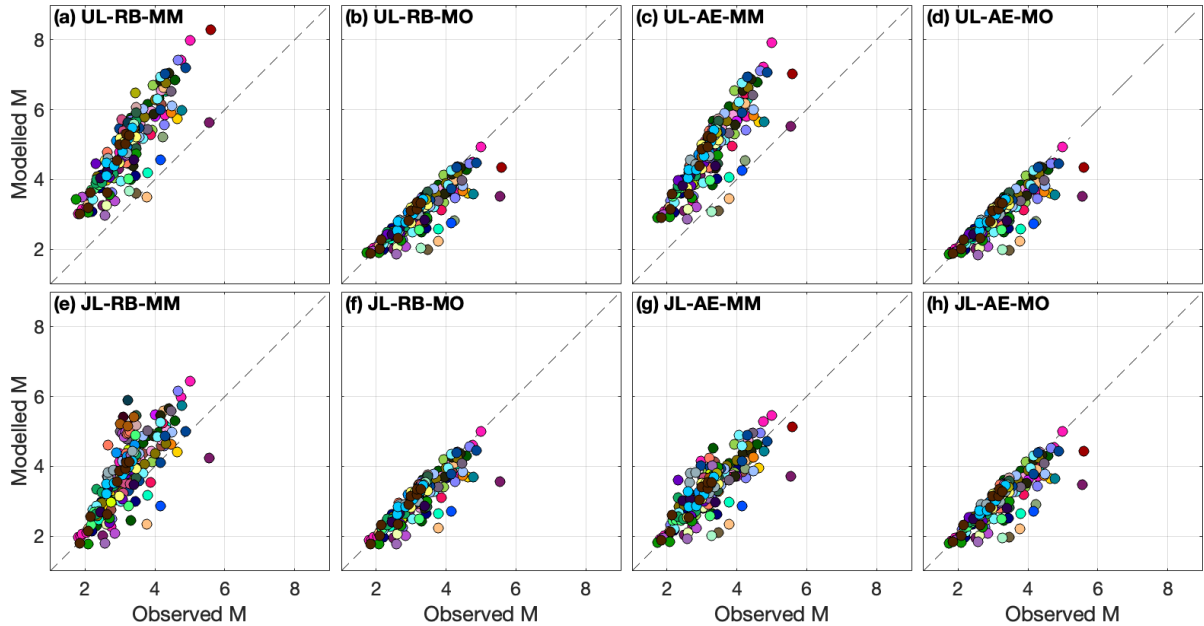
3.4. Application

385 For the OK-KS and WTX datasets we compute M_{NRB} values at intervals of 0.5 months, starting at the
 386 time when at least 10 events above the magnitude of completeness within the sequence have been
 387 recorded, and continuing for the duration of the available catalog. For the W23 sequences, the
 388 timespans of each sequence are highly variable – we therefore compute M_{NRB} values at 1,000 evenly-
 389 spaced intervals between the first and final event within each sequence. At each time step we estimate
 390 the next record breaking magnitude in a pseudo-prospective manner, using all the events in the
 391 sequence that occurred prior to a given time to estimate M_{NRB} for the next time interval.

392 Our objective is to assess the forecast performance as each sequence evolves. We therefore make
 393 comparisons between observed and modelled magnitudes each time there is a new largest event within
 394 the sequence. Each new largest event within the sequence is treated as an observed record-breaking
 395 event, M_{NRB}^0 . The M_{NRB}^0 values are compared against the M_{NRB} values calculated at the timestep prior
 396 to when the M_{NRB}^0 event occurred. For the calculations made using potencies, the modelled values are
 397 converted back to magnitude to facilitate a comparison with the observed magnitudes.

398 4. RESULTS

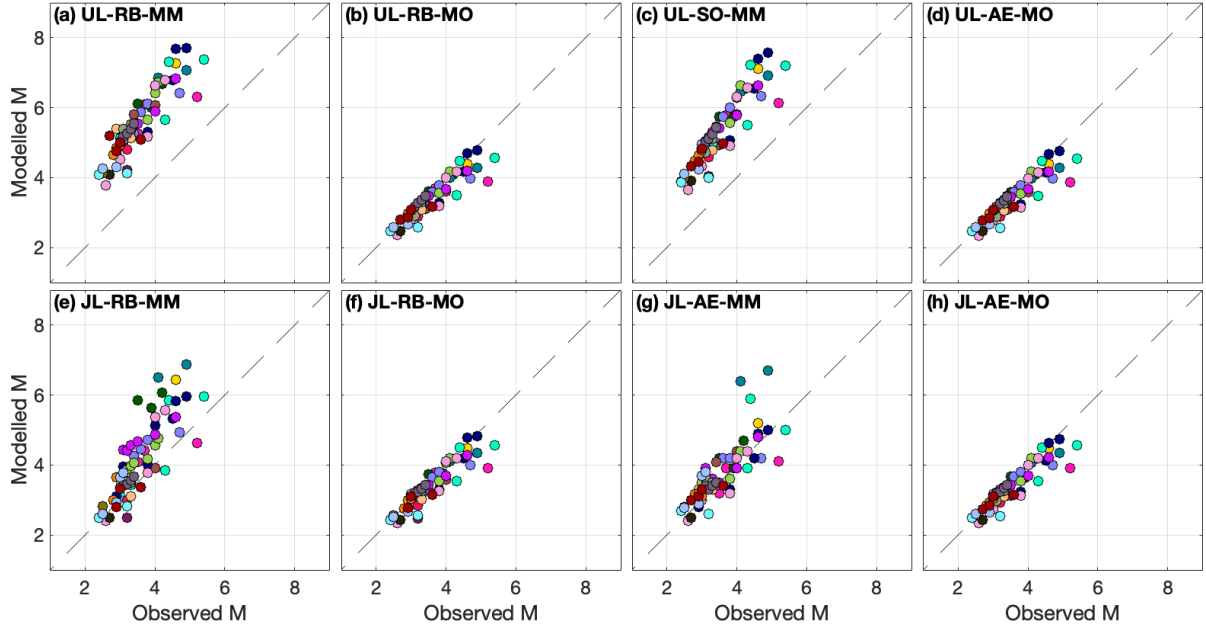
399 Figures 3, 4 and 5 show our results, comparing the observed and forecast M_{NRB}^0 and M_{NRB} values, using
 400 each of the 8 methods described in Table 1, for the sequences from OK-KS (Figure 3), WTX (Figure
 401 4), and the W23 sequences (Figure 5). In total we have applied our models to 86 sequences (48 in OK-
 402 KS, 22 in WTX, 16 from W23), with a combined total of 331 individual record-breaking events within
 403 these sequences (205 from OK-KS, 72 from WTX, 54 from W23). The time evolution of every
 404 individual sequence, and the corresponding modelled M_{NRB} values, are provided in the supplementary
 405 materials (Section S3).



406
 407 *Figure 3: Results for OK-KS sequences comparing observed and modelled magnitudes for each of
 408 the M_{NRB} forecasting methods listed in Table 1. Marker colours correspond to sequences within each
 409 box shown in Figure 1.*

410

411 We quantify the model performance using several metrics. We compute the root-mean-squared (RMS)
 412 error between modelled and observed magnitudes, σ_{RMS} , the Pearson correlation coefficient between
 413 modelled and observed magnitudes, r , and the gradient of the line of (least squares) best-fit, m . A well-
 414 performing model should minimise σ_{RMS} and maximise r , and have a best-fit gradient close to 1.0,
 415 implying a 1:1 relationship between M_{NRB} and M_{NRB}^0 . Additionally, in most applications we anticipate
 416 that M_{NRB} forecasting will be used to guide operational decision making in order to avoid unwanted
 417 large events. It is therefore of particular importance that models do not make large underpredictions,
 418 such that the actual seismicity significantly exceeds what has been forecast by the model. We therefore
 419 compute N_{UP} , the percentage of M_{NRB}^0 instances where the forecast M_{NRB} value was a significant
 420 underprediction with $M_{NRB} < M_{NRB}^0 - 0.5$. These metrics are listed in Table 2 for the OK-KS, WTX
 421 and the W23 sequences respectively.

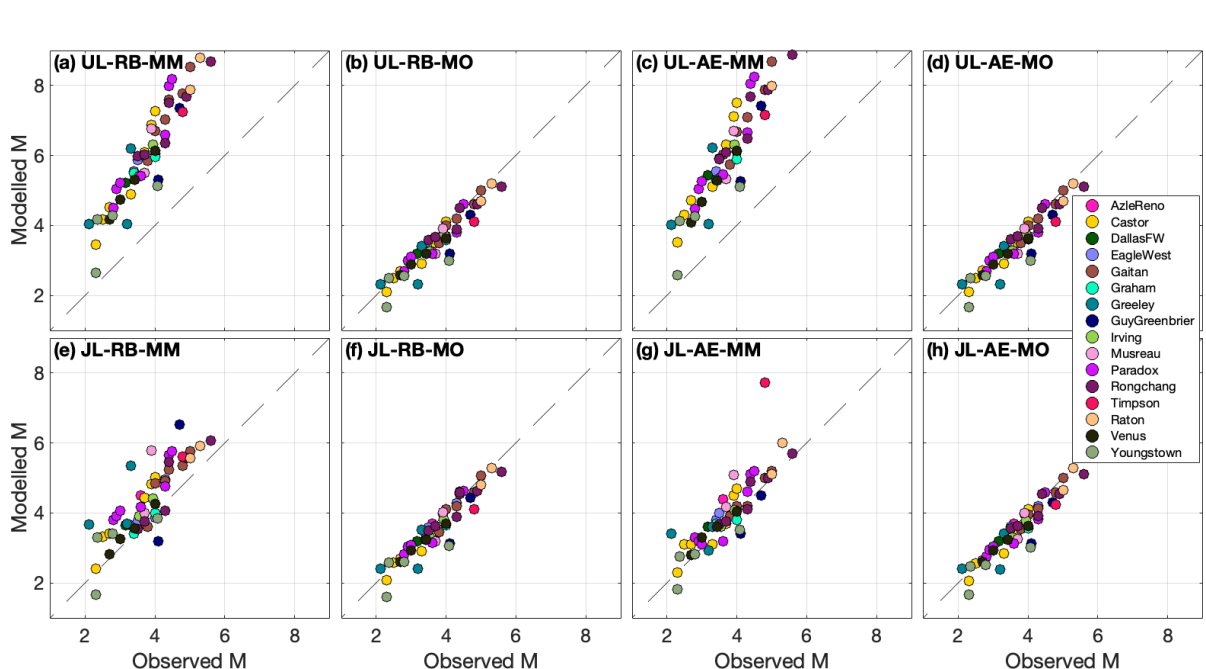


422

423 *Figure 4: Results for WTX sequences comparing observed and modelled magnitudes for each of the*
 424 *M_{NRB} forecasting methods listed in Table 1. Marker colours correspond to sequences within each box*
 425 *shown in Figure 2.*

426

427 In general, we observe strong correlation between the modelled and observed M_{NRB} values, implying
 428 that these methods all provide useful forecasting information for induced seismicity magnitudes, and
 429 could therefore be used as part of a decision-making strategy to manage induced seismicity. The
 430 performance of these models is generally better than that found by Verdon et al. (2024) for commonly
 431 used volume-based forecasting models, having higher correlation coefficients between modelled and
 432 observed magnitudes, lower RMS errors (except for the M_{UL_RB_MM} and M_{UL_RB_MM} models, see below),
 433 and fewer cases where models produced significant underpredictions of upcoming magnitudes.



435

436 *Figure 5: Results for the W23 sequences comparing observed and modelled magnitudes for each of*
 437 *the M_{NRB} forecasting methods listed in Table 1.*

438

439

Table 2: Performance metrics for OK-KS, WTX and W23 sequences.

Model	σ_{RMS}	r	m	N_{UP} [%]
OK-KS				
M _{UL} _RB_MM	1.84	0.86	1.27	0
M _{UL} _RB_MO	0.41	0.86	0.76	14.2
M _{UL} _AE_MM	1.67	0.86	1.24	0
M _{UL} _AE_MO	0.41	0.85	0.76	14.2
M _{JL} _RB_MM	0.93	0.75	1.11	3.4
M _{JL} _RB_MO	0.37	0.87	0.82	12.7
M _{JL} _AE_MM	0.47	0.81	0.85	7.3
M _{JL} _AE_MO	0.41	0.85	0.78	14.6
WTX				
M _{UL} _RB_MM	2.06	0.90	1.23	0
M _{UL} _RB_MO	0.32	0.92	0.78	12.5
M _{UL} _AE_MM	1.84	0.91	1.26	0
M _{UL} _AE_MO	0.32	0.92	0.78	12.5
M _{JL} _RB_MM	0.89	0.83	1.35	2.8
M _{JL} _RB_MO	0.32	0.91	0.81	12.5
M _{JL} _AE_MM	0.54	0.80	0.98	5.6
M _{JL} _AE_MO	0.32	0.91	0.79	12.5
W23				
M _{UL} _RB_MM	2.37	0.93	1.62	0
M _{UL} _RB_MO	0.34	0.94	0.93	11.1
M _{UL} _AE_MM	2.43	0.92	1.66	0
M _{UL} _AE_MO	0.34	0.94	0.93	11.1
M _{JL} _RB_MM	0.81	0.83	1.04	3.7
M _{JL} _RB_MO	0.34	0.93	0.94	11.1
M _{JL} _AE_MM	0.59	0.85	1.05	3.7
M _{JL} _AE_MO	0.34	0.94	0.93	9.3

440

441 More detailed inspection of Figures 3 – 5 and Table 2 leads us to the following conclusions, all of
 442 which are consistent between the OK-KS, WTX, and W23 sequences.

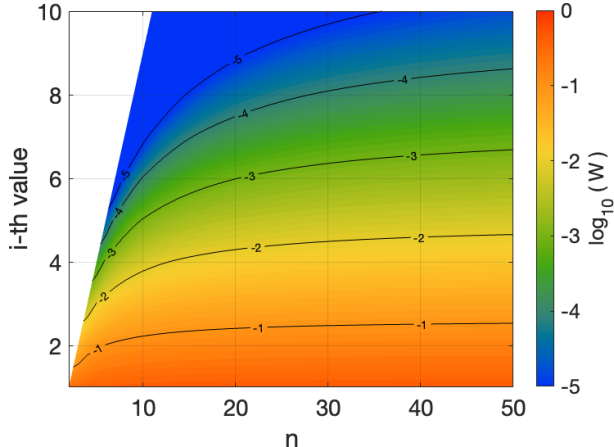
443 **Using re-sorted magnitudes or just record-breaking events does not significantly change**
 444 **forecasting performance.** The use of the entire earthquake catalog, versus solely using record-
 445 breaking events (or jumps to record-breaking events), was a key point of difference between Cao et al.
 446 (2020), Verdon and Bommer (2021) and Watkins et al. (2023) on the one hand, and Cao et al. (2024)
 447 and Schultz et al. (2023a) on the other. However, comparison of panels (a) vs (c), (b) vs (d), (e) vs (g),
 448 and (f) vs (h) of Figures 3 – 5 show that these different implementations in fact produce very similar
 449 results. From examination of Equations 1 and 3 this outcome is unsurprising since only the first few
 450 terms of the weighting applied to the summation of the magnitudes (or jumps), given by:

$$W_i = \left(1 - \frac{i}{n}\right)^n - \left(1 - \frac{i+1}{n}\right)^n \quad (4)$$

451 are significant (Mendecki, 2016). The first weightings correspond to the largest magnitudes (or
 452 magnitude jumps), which tend to be magnitudes (or jumps) that produce record-breaking events.

453 Figure 6 plots the value of W_i as a function of i and n . The weighting term drops to values of 0.01 or
 454 less after the 4th term in the summation (the weighting applied to the 4th-largest magnitude or jump).
 455 The fact that only a few values are required to produce stable magnitude estimates is an additional
 456 advantage of this approach, since it can be applied even where only a few initial events have been
 457 observed in a new sequence.

458



459

460 *Figure 6: Value of the weighting W applied within the summation term in Equations 1 and 3 (as
 461 defined in Equation 4) as a function of i . The contours here show values of $\log_{10}(W)$. For any value
 462 of n , the weighting for terms where $i > 4$ is less than 0.01.*

463

464 **Upper limit models using magnitude provide a credible upper limit.** The $M_{UL_AE_MM}$ and $M_{UL_RB_MM}$
 465 models (panels (a) and (c) in Figures 3 – 5) did not produce any significant underpredictions ($N_{UP} = 0$).
 466 This is notable given that we have applied it to 86 individual earthquake sequences. Hence, the
 467 UL_MM values (upper limit calculations using magnitudes) do seem to provide a credible upper limit
 468 to induced earthquake magnitudes.

469 However, while these values never produced underpredictions, they did not provide a good fit to the
 470 evolution of record-breaking magnitudes within sequences, tending to produce significant
 471 overpredictions in most cases. This is to be expected since the M_{UL} method is formulated to estimate
 472 the largest possible value within a distribution, not the expected next record-breaking event. As a
 473 result, the $M_{UL_AE_MM}$ and $M_{UL_RB_MM}$ models gave the largest σ_{RMS} values, and best-fit relationships with
 474 the gradient m significantly higher than 1.0. That said, the correlation coefficients for the $M_{UL_AE_MM}$
 475 and $M_{UL_RB_MM}$ models are not significantly worse than those of other models, implying that the scatter
 476 between modelled and observed magnitudes is no worse than for the other models, just the fit is not
 477 along the 1:1 line, resulting in systematic overprediction.

478 **Next record-breaking models using magnitudes produce the highest scatter.** Although the
 479 $M_{JL_AE_MM}$ and $M_{JL_RB_MM}$ models (panels (e) and (g) in Figures 3 – 5) produced reasonable fits between
 480 observed and modelled magnitudes, with the gradient m close to 1.0, these models had the lowest
 481 correlation coefficients of all the models, and the highest σ_{RMS} values with the exception of the
 482 overpredicting $M_{UL_AE_MM}$ and $M_{UL_RB_MM}$ models, as described above. The $M_{JL_AE_MM}$ and $M_{JL_RB_MM}$
 483 models therefore produced the highest scatter between modelled and observed magnitudes and may
 484 therefore have the least utility in forecasting. This is ironic given that this approach has been the most
 485 widely used to date, forming the basis of results presented by Cao et al. (2020; 2024), Verdon and
 486 Bommer (2021), Watkins et al. (2023) and Schultz et al. (2023a).

487 **Potency-based models have the least scatter, but significantly underpredict on occasion.** All four
 488 of the models that used earthquake potencies, $M_{UL_AE_MO}$, $M_{UL_RB_MO}$, $M_{JL_AE_MO}$, and $M_{JL_RB_MO}$ (panels
 489 (b), (d), (f) and (h) in Figures 3 – 5) produced very similar results. These models had the lowest σ_{RMS}
 490 values and highest correlation coefficients, indicating that these models had low scatter and the closest
 491 match between modelled and observed magnitudes. However, these models also produced the largest
 492 number of underpredictions, with between 10 – 15 % of events being underpredicted by more than 0.5
 493 magnitude units. We surmise that in most cases where sequences are evolving relatively gently, the
 494 potency-based models perform well. However, they do not perform as well in capturing the more
 495 unusual sequences where a sharp increase in magnitudes takes place.

496 5. DISCUSSION

497 5.1. Towards an empirically constrained probabilistic model

498 Our results show that the upper limit magnitude-based models, $M_{UL_AE_MM}$ and $M_{UL_RB_MM}$, provided
 499 credible upper bounds for the actual event magnitudes, having no significant underpredictions after
 500 application to a large number of sequences. However, in most cases these models overpredicted the
 501 observed events. In contrast, the potency-based models ($M_{UL_AE_MO}$, $M_{UL_RB_MO}$, $M_{JL_AE_MO}$, and
 502 $M_{JL_RB_MO}$) generally produced a good fit to the observed magnitudes, but occasionally produced
 503 significant underpredictions.

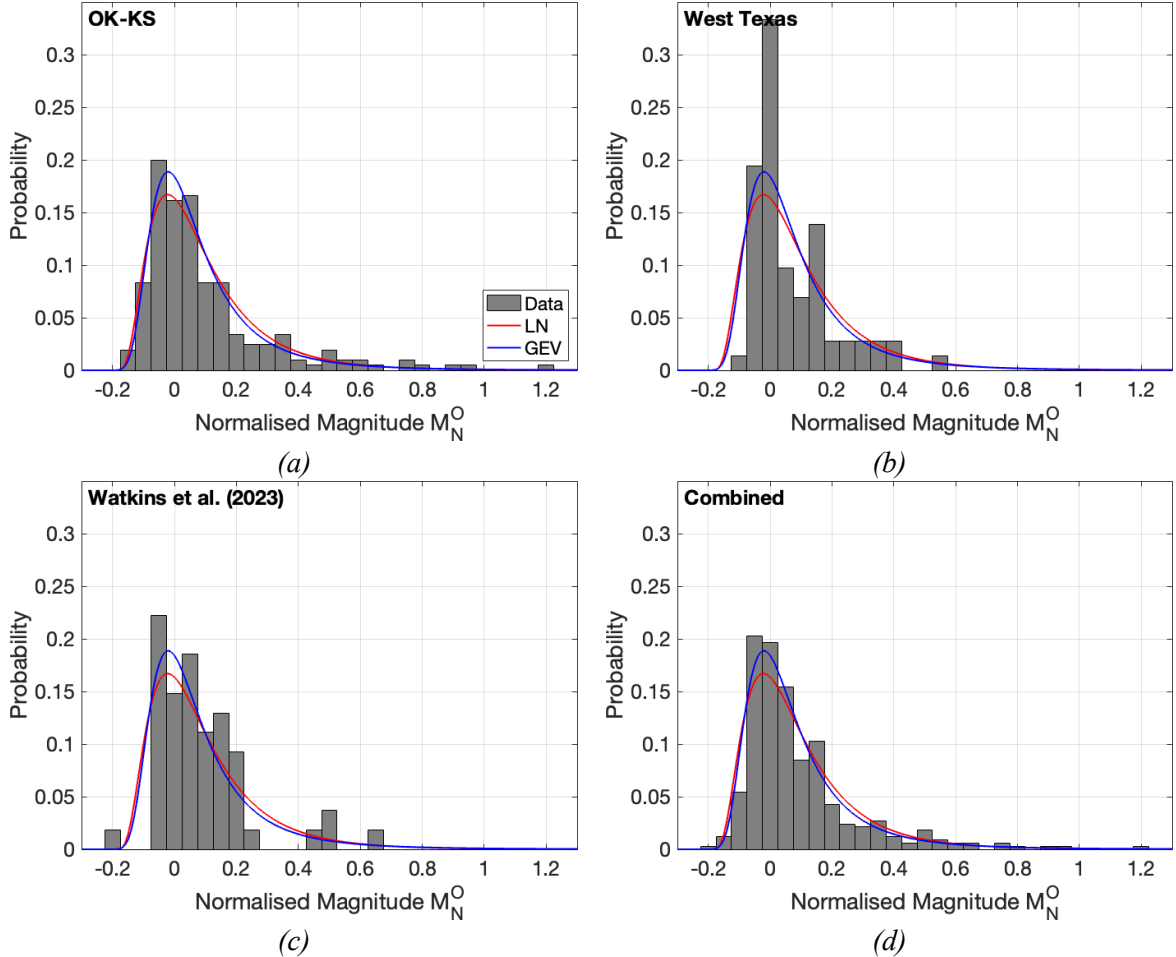
504 From this, it is reasonable to propose a composite approach to forecasting event magnitudes where
 505 $M_{UL_AE_MM}$ or $M_{UL_RB_MM}$ is used provide an upper estimator for the expected magnitude of the next
 506 record-breaking event and $M_{UL_AE_MO}$, $M_{UL_RB_MO}$, $M_{JL_AE_MO}$, or $M_{JL_RB_MO}$ is used to provide a lower
 507 estimator for the expected magnitude. Hereafter, we use $M_{UL_RB_MM}$ for the upper estimator and
 508 $M_{JL_AE_MO}$ for the lower estimator, referred to hereafter as M_{UE} and M_{LE} respectively.

509 The probability distribution of event magnitudes between these estimators can be evaluated through
 510 empirical calibration with our observed seismicity. For each event, we normalise each observed record-
 511 breaking event magnitude relative to the M_{LE} and M_{UE} estimators at the time of the event's occurrence:

$$512 M_N^O = \frac{M_{NRB}^O - M_{LE}}{M_{UE} - M_{LE}} \quad (5)$$

513 We then examine the distribution of these normalised magnitudes – where do events typically fall with
 514 respect to the upper and lower magnitude estimators? Our results for each of our studies are shown in
 515 Figure 7. The distributions of M_N^O are consistent between the three sets of sequences that we studied.
 516 Most values are close to 0, i.e., they match the modelled lower estimator values, $M_{NRB}^O = M_{LE}$.
 517 However, the distribution has a tail of higher values extending towards 1, i.e., where observed
 magnitudes reach towards the higher estimator values, $M_{NRB}^O = M_{UE}$.

518 We examine the fit of various statistical distributions to our observations, including lognormal, a
 519 Gumbel, and Generalised Extreme Value (GEV) distributions. We further test the performance of these
 520 distributions when applied to synthetically generated sequences. These results are shown in our
 521 Supplementary Materials (Sections S1 and S2). The consistency found for M_N^O between our different
 522 case studies and synthetic models enables us to construct an empirically constrained probabilistic
 523 model for induced seismicity forecasting using extreme value estimators. We find that our observations
 524 are reasonably approximated either by a shifted lognormal distribution with a mean of $\mu_{LN} = -1.4$, a
 525 deviation of $\sigma_{LN} = 0.6$, and a shift of $\delta_{LN} = 0.2$, or a GEV distribution with shape parameter $k_{GEV} = 0.23$,
 526 scale parameter $\sigma_{GEV} = 0.1$, and location parameter $\mu_{GEV} = 0.0$. Hereafter we use the GEV distribution
 527 as providing the best fit to our combined observations (see Supplementary Materials Section S1).



528 *Figure 7: Distribution of normalised observed magnitudes M_N^O (bars), where the observed*
529 *magnitudes are normalised relative to the modelled upper and lower estimators, for the OK-KS (a),*
530 *WTX (b), and W23 (c) sequences, and for all observations combined (d). The red and blue lines show*
531 *the shifted lognormal and GEV distributions that we adopt to approximate the observed*
532 *distributions.*

533
534 For a given sequence of seismicity, we compute the M_{UE} and M_{LE} estimators at a given time. Having
535 computed M_{UE} and M_{LE} , we can compute the probabilities for the next largest magnitude event that
536 will occur in the sequence. We use Equation 5 to normalise magnitudes relative to M_{UE} and M_{LE} , and
537 then estimate the probability of occurrence for any magnitude event from the GEV distribution with
538 scale, shape and location parameters described above.

539 Our synthetic testing (Supplementary Materials Section S2) shows that the observed distributions are
540 consistent with situations where no upper truncation is applied to the G-R distribution from which the
541 events are drawn (or where the magnitude of truncation is much larger than the observed event sizes,
542 such that this has, in effect, no impact on the simulated magnitudes). Where a truncation is applied to
543 our synthetic tests, the M_N^O values are systematically shifted towards the lower estimator ($M_N^O = 0$),
544 such that the representative distributions defined above are no longer appropriate. The similarities
545 between our observed distributions and those generated by an untruncated model, alongside past
546 studies which have generally failed to find significant evidence for magnitude truncations in most
547 induced seismicity cases (e.g., van der Elst et al., 2016) suggest that our approach is reasonable with
548 respect to this caveat. However, if clear upper truncations to the G-R distribution are observed for
549 induced seismicity sequences (e.g., Verdon et al., 2018), then alternative methods for M_{MAX} estimation,

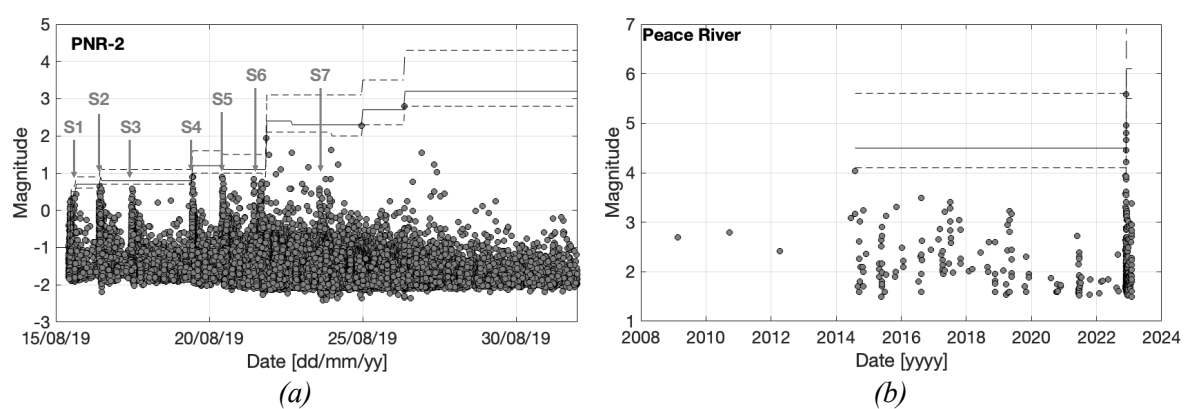
550 such as those that explicitly assume an upper-truncated G-R distribution (e.g., Kijko and Sellevoll,
551 1989; Pisarenko et al., 1996; Holschneider et al., 2011), may be preferable.

553 **5.2. Application to out-of-sample cases**

554 We demonstrate this approach by application to two notable cases of induced seismicity: from
555 hydraulic fracturing at the Preston New Road PNR-2 well in Lancashire, England in 2019 (Kettlety et
556 al., 2021), and from seismicity associated with WWD activities in north-western Alberta, near to the
557 town of Peace River (Schultz et al., 2023b). The PNR-2 sequence is notable because its occurrence led
558 the UK government to impose a moratorium on hydraulic fracturing, primarily because of the
559 perceived inability to “accurately predict the probability or magnitude of earthquakes linked to
560 fracking operations” (BEIS, 2019).

561 The Peace River sequence reached a magnitude of $M 5.6$ in November 2022. If induced (the nature of
562 this event is still disputed, see Salvage et al., 2024) it would be the largest magnitude induced event in
563 the Western Canada Sedimentary Basin. This sequence is useful for our purposes since, given when it
564 occurred, it was not included in the sequences compiled by Watkins et al. (2023), and so it represents
565 an out-of-sample test, since the sequences in W23 were used to generate our empirically constrained
566 distribution of M^O_N .

567 For the PNR-2 sequence, we use the corrected moment magnitudes published by Kettlety and Butcher
568 (2022) – note that these M_W values are different from the M_L values published by Kettlety et al. (2021).
569 For the Peace River sequence, we use earthquakes from the Alberta Geological Survey database (AGS,
570 2020). Our results are shown in Figure 8, where the observed seismicity is compared with the forecast
571 values. The solid lines in Figure 8 show the magnitude that has a 50 % chance of exceedance by the
572 next record-breaking event, M_{50} , while the dashed lines show M_{95} and M_{05} (i.e., the magnitude that has
573 a 95 % chance of being exceeded, and the magnitude that has a 5 % chance of being exceeded by the
574 next record-breaking event).



576 *Figure 8: Application of the empirically constrained forecasting model to the Preston New Road*
577 *PNR-2 (a) and Peace River (b) sequences. Observed events are marked with grey dots. The solid line*
578 *marks M_{50} , while the dashed lines mark M_{05} and M_{95} . For PNR-2, the bursts of seismicity associated*
579 *with each discrete hydraulic fracturing interval (Stages 1-7) are marked with grey arrows.*

580
581 For the Peace River case, the forecast values are stable for the duration of the sequence. The $M 5.6$
582 event that occurs is close to the M_{05} value, indicating a 5 % likelihood of this magnitude being reached
583 or exceeded.

584 For PNR-2, the M 2.8 event is well within the forecast range, and close to the M_{50} value at the time it
585 occurred. Hydraulic fracturing at PNR-2 was conducted as a series of discrete injection stages,
586 typically lasting between 1 – 2 hours, with only one injection stage taking place each day. Stage 7 was
587 the last stage to have been stimulated, with the M 2.8 event occurring roughly 72 hours after this stage
588 had been completed (Kettlety et al., 2021). The forecast values prior to Stage 7 are therefore of
589 particular interest since these values could have informed the operational decision to perform this
590 stage. At the time that injection of Stage 7 began, the likelihood of reaching or exceeding M 2.8 was
591 12 %. The forecasting model therefore provides a reasonable characterisation of the hazard at the time
592 that the decision to proceed with Stage 7 was made.

593 Interestingly, the event that most exceeds the forecast is the M 1.9 event that followed Stage 6. At the
594 start of injection of Stage 6, the likelihood of reaching or exceeding M 1.9 was only 1 %. Kettlety et
595 al. (2021) identified that Stage 6 saw a significant change in geomechanical behaviour in the reservoir,
596 with microseismicity beginning to occur along the fault structure that ultimately hosted the M 2.8
597 event. Kettlety et al. (2021) interpreted the microseismicity prior to Stage 6 as being associated with
598 hydraulic fracture propagation (and the reactivation of some natural fracture networks), whereas
599 microseismicity from Stage 6 onwards begins to represent the onset of reactivation of a critically
600 stressed fault.

601 This highlights one of the challenges with induced seismicity forecasting – where a sudden change in
602 the underlying geomechanical behaviour takes place, events from prior to this change may not be
603 useful in forecasting subsequent behaviour. As described in our Methods, the M_{UL} and M_{JL} estimators
604 assume that record-breaking magnitudes are sampled from a stationary underlying distribution. We
605 note that this caveat also applies to other induced seismicity forecasting methods that assume constant
606 scaling between injection rates and induced seismicity rates (e.g., Shapiro et al., 2010; Hallo et al.,
607 2014; Mancini et al., 2021).

608 It is unclear the degree to which this assumption should be expected to hold for induced seismicity
609 sequences. For WWD, injection rates are typically constant over years, creating a slow and steady
610 pressure increase, such that a relatively constant underlying distribution of seismicity might be
611 expected. However, Verdon et al. (2024) found evidence for accelerating rates of seismicity relative
612 to injection volumes during the early stages of WWD-induced seismicity onset, which then stabilised
613 at later times.

614 The successful performance of the M_{UL} and M_{JL} estimators in our study suggests that the assumption
615 of stationarity is sufficiently satisfied, at least on the timescale of intervals between record-breaking
616 events in these WWD-induced sequences. In contrast, for hydraulic fracturing at PNR-2, the
617 microseismicity associated with hydraulic fracture propagation during the earlier stages does not do a
618 good job of forecasting what happened as the larger fault began to reactivate. Once this fault
619 reactivated, the forecasting model using the seismicity from this point onwards does a good job of
620 forecasting the subsequent seismicity that developed.

621 These observations show that care should be taken to fully interpret and understand the geomechanical
622 behaviours that can be manifested in microseismic event observations when using statistical models
623 to forecast induced seismicity. It may be necessary to assess whether the underlying assumptions –
624 such as stationarity and constancy of scaling between injection rate and seismicity rate – are reasonable
625 in a particular case. These assumptions may not be appropriate in situations, such as at PNR-2, where
626 a new fault structure is encountered by a growing injection pulse and begins to reactivate.

628 **5.3. Time dependent forecasting**

629 The forecasting methods developed here do not provide any estimate of whether a new record-breaking

630 event will occur and, if so, when it will occur. The timing of the next record-breaking event could be
631 estimated from the growing number of earthquakes within a sequence. The expected number of record-
632 breaking events, N_{rb} , in a population of n events can be approximated, assuming that the events are
633 independent and drawn from a constant underlying distribution, as (Arnold et al., 1998; Nevzorov,
634 2001):

$$N_{rb} \approx \ln(n) + 0.577215 \quad (6)$$

635 with the variance given by:

$$\text{Var}(N_{rb}) = \ln(n) - 1.0677 \quad (7)$$

636 The number of record-breaking events relative to the total number of events within the sequence could
637 therefore be used to indicate whether another record-breaking event might be imminent. Further
638 investigation of this possibility is clearly merited.

639 Perhaps more importantly, the methods developed here, which are based on the concept of record-
640 breaking events, imply that M_{MAX} for a sequence of induced seismicity will be ever-increasing, unless
641 and until clear evidence of an upper truncation to the G-R distribution emerges. In practice, many
642 sequences of induced seismicity generated by long-term injection have shown time-dependent
643 behaviour where magnitudes increased during the first years of injection, but then stabilised and
644 decreased over time (Rodríguez-Pradilla et al., 2022; Watkins et al., 2023; Verdon et al., 2024).

645 As sequences stabilise and abate, magnitude forecasts based on extreme value estimators will cease to
646 be appropriate. Clearly, some means of estimating the point at which the rates and magnitudes of
647 induced seismicity are no longer increasing is required. One method may be to compare the numbers
648 of record-breaking events when the sequence is run forwards versus when the sequence is run in a
649 time-reversed order (Mendecki, 2016). If the earthquake sequence is sampling from an underlying
650 stationary distribution, then we would expect the same number of record-breaking events whether the
651 sequence is run forwards or backwards. If there are significantly more record-breaking events when
652 the sequence is run forwards, then this would imply that the hazard is increasing, while if there are
653 significantly more record-breaking events when the sequence is run in reverse, then this would imply
654 that the hazard is abating. Again, further investigation of this concept is clearly merited.

655 6. CONCLUSIONS

656 We have assessed the performance of induced seismicity forecasting models for M_{NRB} using methods
657 based on extreme value estimators. These models can be implemented in a number of different ways,
658 and we have quantitatively compared the performance of these implementations. We compiled a
659 database of over 80 individual sequences of induced seismicity against which comparisons of model
660 performance were made. We found that using all events within a catalog or just the record-breaking
661 events made little difference to the forecasting results, since the models are primarily sensitive to the
662 largest magnitude events in the sequence.

663 Estimates of M_{NRB} using the upper limit method with event magnitudes tended to overestimate the
664 observed magnitudes. However, unlike other models, this model never significantly underpredicted
665 the observed seismicity, so it has use in defining an upper estimate for M_{NRB} . The models which used
666 earthquake potency instead of magnitude produced the closest overall fit to the observed magnitudes,
667 but on occasion did produce significant underestimates of the observed magnitudes. The potency-
668 based models seldom produced overpredictions of the observed magnitudes.

669 Based on these observations, we conclude that the upper limit magnitude-based model and the jump-
670 limited potency-based models can be combined to give upper and lower estimators for the upcoming
671 events within an induced seismicity sequence. We found that most of the observed events were much

672 closer to the lower magnitude estimator. We used these observations to define an empirically
673 constrained probability distribution for expected magnitudes relative to the upper and lower estimators.
674 This distribution was consistent between the different populations of induced seismicity sequences
675 compiled for our analysis, as well as for sequences that were generated synthetically.

676 We applied this forecasting approach to two out-of-training-sample (i.e., not used in defining our
677 empirically constrained distribution) sequences of induced seismicity. We find that in both cases our
678 modelling approach does a good job of characterising the induced seismicity that occurred. However,
679 the example from PNR-2 again highlights one of the major challenges in forecasting induced
680 seismicity: where rapid changes in the underlying geomechanical processes occur (such as when a
681 different fault begins to be perturbed), seismicity from earlier within the sequence may not be useful
682 for forecasting once this change has occurred.

683

684 **Data and Resources**

685 The earthquake catalog for Oklahoma was sourced from Park et al. (2022), where the catalog is
686 provided as a digital supplement. The earthquake catalog for Texas was sourced from the TexNet
687 database at <https://www.beg.utexas.edu/texnet-cisr/texnet/earthquake-catalog> (last accessed
688 14/02/2024). The earthquake catalogs for the sequences described by Watkins et al. (2023) are
689 available as a digital supplement to that paper. The catalog for PNR-2 is available from the UK
690 National Geoscience Data Centre at
691 <https://webapps.bgs.ac.uk/services/ngdc/acquisitions/index.html#item173104> (last accessed
692 14/02/2024). The catalog for the Peace River sequence was sourced from the Alberta Earthquake
693 Dashboard at https://ags-aer.shinyapps.io/Seismicity_waveform_app/ (last accessed 14/02/2024).

694

695 **Acknowledgements**

696 JPV's contribution to this research was funded by the NERC SeisGreen grant (Grant Number
697 NE/W009293/1). We are grateful to Dr Robert Shcherbakov and an anonymous reviewer for their
698 thorough and constructive reviews of our original manuscript.

699

700 References

701 AGS, 2020. Alberta Earthquake Dashboard: Alberta Geological Survey. Available at: <https://ags.aer.ca/publication/iam-005>
702 (last accessed 14/02/2024).

703 Arnold, B.C., N. Balakrishnan, H.N. Nagaraja, 1998. Records. John Wiley and Sons, New York.

704 BEIS, 2019. Government ends support for fracking: Press Release from the UK Department of Business, Energy and
705 Industrial Strategy. Available at: <https://www.gov.uk/government/news/government-ends-support-for-fracking> (last
706 accessed 15/08/2023).

707 Block, L.V., C.K. Wood, W.L. Yeck, V.M. King, 2014. The 24 January 2013 M_L 4.4 earthquake near Paradox, Colorado,
708 and its relation to deep well injection: *Seismological Research Letters* 85, 609-624.

709 Bommer, J.J., 2022. Earthquake hazard and risk analysis for natural and induced seismicity: towards objective assessments
710 in the face of uncertainty: *Bulletin of Earthquake Engineering* 20, 2825-3069.

711 Campbell, N.M., M. Leon-Corwin, L.A. Ritchie, J. Vickery, 2020. Human-induced seismicity: risk perceptions in the state
712 of Oklahoma: *The Extractive Industries and Society* 7, 119-126.

713 Cao, N-T., L. Eisner, Z. Jechumtálková, 2020. Next record-breaking magnitude for injection induced seismicity: *First Break*
714 38, 53-57.

715 Cao, N-T., L. Eisner, Z. Jechumtálková, J.P. Verdon, U. bin Waheed, 2024. Upper limit magnitudes for induced seismicity in
716 energy industries: *Geophysical Prospecting*, accepted.

717 Cesca, S., D. Stich, F. Grigoli, A. Vuan, J.Á. López-Comino, P. Niemz, E. Blanch, T. Dahm, W.L. Ellsworth, 2021. Seismicity at the Castor gas reservoir driven by pore pressure diffusion and asperities loading: *Nature Communications*
718 12, 4783.

720 Clarke, H., J.P. Verdon, T. Kettlety, A.F. Baird, J-M. Kendall, 2019. Real time imaging, forecasting and management of
721 human-induced seismicity at Preston New Road, Lancashire, England: *Seismological Research Letters* 90, 1902-1915.

722 Clauzet, A., C.R. Shalizi, M.E.J. Newman, 2009. Power-law distributions in empirical data: *Society of Industrial and Applied*
723 *Mathematics Reviews* 51, 661-703.

724 Cooke, P., 1979. Statistical inference for bounds of random variables: *Biometrika* 66, 367-374.

725 Davis, S.D., and W.D. Pennington, 1989. Induced seismic deformation in the Cogdell oil field of west Texas: *Bulletin of the*
726 *Seismological Society of America* 79, 1477-1494.

727 Dempsey, D. and J. Suckale, 2017. Physics-based forecasting of induced seismicity at Groningen gas field, the Netherlands: *Geophysical Research Letters* 44, 7773-7782.

729 Eaton, D.W., and N. Igonin, 2018. What controls the maximum magnitude of injection-induced earthquakes: *The Leading*
730 *Edge* 37, 135-140.

731 Eaton, D.W., N. Igonin, A. Poulin, R. Weir, H. Zhang, S. Pellegrino, G. Rodriguez, 2018. Induced seismicity characterization
732 during hydraulic-fracture monitoring with a shallow-wellbore geophone array and broadband sensors: *Seismological*
733 *Research Letters* 89, 1641-1651.

734 Evensen, D., A. Varley, L. Whitmarsh, P. Devine-Wright, J. Dickie, P. Bartie, H. Napier, I. Mosca, C. Foad, S. Ryder, 2022. Effect of linguistic framing and information provision on attitudes towards induced seismicity and seismicity regulation: *Scientific Reports* 12, 11239.

737 Frohlich, C., W. Ellsworth, W.A. Brown, M. Brunt, J. Luetgert, T. MacDonald, S. Walter, 2014. The 17 May 2012 M 4.8 earthquake near Timpson, East Texas: An event possibly triggered by fluid injection: *Journal of Geophysical Research*
738 119, 581-593.

740 Grigoratos, I., A. Savvaidis, E. Rathje, 2022. Distinguishing the causal factors of induced seismicity in the Delaware basin: hydraulic fracturing or wastewater disposal: *Seismological Research Letters* 93, 2640-2658.

742 Gutenberg, B., and C.F. Richter, 1944. Frequency of earthquakes in California: *Bulletin of the Seismological Society of*
743 *America* 34, 185-188.

744 Hallo, M., I. Oprsal, L. Eisner, M.Y. Ali, 2014. Prediction of magnitude of the largest potentially induced seismic event: *Journal of Seismology* 18, 421-431.

746 Holland, A.A., 2013. Earthquakes Triggered by Hydraulic Fracturing in South-Central Oklahoma: *Bulletin of the*
747 *Seismological Society of America* 103, 1784-1792.

748 Hennings, P.H., and M.H. Young, 2023. The TexNet-CISR collaboration and steps toward understanding induced seismicity in Texas: in R.C. Buchanan, M.H. Young, K.E. Murray eds., *Recent Seismicity in the Southern Midcontinent, USA: Scientific, Regulatory, and Industry Responses*: Geological Society of America Special Paper 559, 53-71.

751 Hennings, P.H., J.P. Nicot, R.S. Gao, H.R. DeShon, J.E. Lund Snee, A.P. Morris, M.R. Brudzinski, E.A. Horne, C. Breton,
752 2021. Pore pressure threshold and fault slip potential for induced earthquakes in the Dallas-Fort Worth area of north
753 central Texas: *Geophysical Research Letters* 48, e2021GL093564.

754 Holschneider, M., G. Zöller, S. Hainzl, 2011. Estimation of the maximum possible magnitude in the framework of a doubly
755 truncated Gutenberg-Richter model: *Bulletin of the Seismological Society of America* 101, 1649-1659.

756 Horton, S., 2012. Injection into subsurface aquifers triggers earthquake swarm in central Arkansas with potential for
757 damaging earthquake: *Seismological Research Letters* 83, 250-260.

758 Horner, R.B., J.E. Barclay, J.M. MacRae, 1994. Earthquakes and hydrocarbon production in the Fort St. John area of
759 northeastern British Columbia: *Canadian Journal of Exploration Geophysics* 30, 39-50.

760 Hosseini, B.K., and D.W. Eaton, 2018. Fluid flow and thermal modeling for tracking induced seismicity near the Graham
761 disposal well, British Columbia (Canada): *SEG 88th Annual Conference, Anaheim CA, Expanded Abstracts* 4987-4991.

762 Keranen, K.M., H.M. Savage, G.A. Abers, E.S. Cochran, 2013. Potentially induced earthquakes in Oklahoma: USA: links
763 between wastewater injection and the 2011 M_W 5.7 earthquake sequence: *Geology* 41, 699-702.

764 Kettlety, T., and A. Butcher, 2022. Local and moment magnitudes of Preston New Road seismicity, 2018-2019: National
765 Geological Data Centre, DOI: 10.5285/709cbc2f-af5c-4d09-a4ea-6deb5aa8c5d8.

766 Kettlety, T., J.P. Verdon, A. Butcher, M. Hampson, L. Craddock, 2021. High-resolution imaging of the M_L 2.9 August 2019
767 earthquake in Lancashire, United Kingdom, induced by hydraulic fracturing during Preston New Road PNR-2
768 operations: *Seismological Research Letters* 92, 151-169.

769 Kijko, A., 2004. Estimation of the maximum earthquake magnitude, m_{max} : *Pure and Applied Geophysics* 161, 1655-1681.

770 Kijko, A., and M.A. Sellevoll, 1989. Estimation of earthquake hazard parameters from incomplete data files. Part I:
771 Utilization of extreme and complete catalogs with different threshold magnitudes: *Bulletin of the Seismological Society
772 of America* 79, 645-654.

773 Kim, W.-Y., 2013. Induced seismicity associated with fluid injection into a deep well in Youngstown, Ohio: *Journal of
774 Geophysical Research* 118, 3506-3518.

775 Kwiatek, G., T. Saamo, T. Ader, F. Bluemle, M. Bohnhoff, M. Chendorain, G. Dresen, P. Heikkinen, I. Kukkonen, P. Leary,
776 M. Leonhardt, P. Malin, P. Martinez-Garzon, K. Passmore, P. Passmore, S. Valenzuela, C. Wollin, 2019. Controlling
777 fluid-induced seismicity during a 6.1-km-deep geothermal stimulation in Finland: *Science Advances* 5, eaav7224.

778 Lee, K.K., W.L. Ellsworth, D. Giardini, J. Townend, S. Ge, T. Shimamoto, I-W. Yeo, T-S. Kang, J. Rhie, D-H. Sheen, C.
779 Chang, J-U. Woo, C. Langenbruch, 2019. Managing injection-induced seismic risks: *Science* 364, 730-732.

780 Lei, X., Z. Wang, J. Su, 2019. The December 2018 M_L 5.7 and January 2019 M_L 5.3 earthquakes in south Sichuan Basin
781 induced by shale gas hydraulic fracturing: *Seismological Research Letters* 90, 1099-1110.

782 Li, T., Y.J. Gu, J. Wang, R. Wang, J. Yusifbayov, M. Reyes Canales, T. Shipman, 2022. Earthquakes induced by wastewater
783 disposal near Musreau Lake, Alberta, 2018-2020: *Seismological Research Letters* 93, 727-738.

784 Mancini, S., M.J. Werner, M. Segou, B. Baptie, 2021. Probabilistic forecasting of hydraulic fracturing-induced seismicity
785 using an injection-rate driven ETAS model: *Seismological Research Letters* 92, 3471-3481.

786 McGarr, A., 1976. Seismic moments and volume changes: *Journal of Geophysical Research* 81, 1487-1494.

787 Mendecki, A.J., 2016. *Mine Seismology Reference Book*. Institute of Mine Seismology, Somerset West, South Africa.

788 Molina, I., J.S. Velásquez, J.L. Rubenstein, A. Garcia-Aristizabal, V. Dionicio, 2020. Seismicity induced by massive
789 wastewater injection near Puerto Gaitán, Colombia: *Geophysical Journal International* 223, 777-781.

790 Mueller C.S., 2010. The influence of maximum magnitude on seismic-hazard estimates in the central and eastern United
791 States: *Bulletin of the Seismological Society of America* 100, 699-711.

792 Nakai, J.S., M. Weingarten, A.F. Sheehan, S.L. Bilek, S. Ge, 2017. A possible causative mechanism of Raton Basin, New
793 Mexico and Colorado earthquakes using recent seismicity patterns and pore pressure modelling: *Journal of Geophysical
794 Research* 122, 8051-8065.

795 Nantanoi, S., G. Rodríguez-Pradilla, J.P. Verdon, 2022. 3D-seismic interpretation and fault slip potential analysis from
796 hydraulic fracturing in the Bowland Shale, UK: *Petroleum Geoscience* 28, petgeo2021-057.

797 Nevezorov, V.B., 2001. *Records: Mathematical Theory*. American Mathematical Society, Providence, Rhode Island.

798 Park, Y., G.C. Beroza, W.L. Ellsworth, 2022. Basement fault activation before larger earthquakes in Oklahoma and Kansas:
799 *The Seismic Record* 2, 197-206.

800 Pisarenko, V.F., A.A. Lyubushin, V.B. Lysenko, T.V. Golubeva, 1996. Statistical estimation of seismic hazard parameters:
801 Maximum possible magnitude and related parameters: *Bulletin of the Seismological Society of America* 86, 691-700.

802 Rodríguez-Pradilla, G., D.W. Eaton, J.P. Verdon, 2022. Basin-scale multi-decadal analysis of hydraulic fracturing and
803 seismicity in western Canada shows non-recurrence of induced runaway fault-rupture: *Scientific Reports* 12, 14463.

804 Rubenstein, J.L., and A.B. Mahani, 2015. Myths and facts on wastewater injection, hydraulic fracturing, enhanced oil
805 recovery, and induced seismicity: *Seismological Research Letters* 86, 1060-1067.

806 Rutqvist, J., A.P. Rinaldi, F. Cappa, G.J. Moridis, 2013. Modeling of fault reactivation and induced seismicity during
807 hydraulic fracturing of shale-gas reservoirs: *Journal of Petroleum Science and Engineering* 107, 31-44.

808 Salvage, R.O., D.W. Eaton, C.M. Furlong, J. Dettmer, P.K. Pedersen, 2024. Induced or natural? Toward rapid expert
809 assessment, with application to the M_w 5.2 Peace River earthquake sequence: *Seismological Research Letters* 95, 758-
810 772.

811 Savvaidis, A., B. Young, G.D. Huang, A. Lomax, 2019. TexNet: A statewide seismological network in Texas: *Seismological
812 Research Letters* 90, 1702-1715.

813 Schultz, R., Y. Park, A. Leonardo, A. Suarez, W.L. Ellsworth, G.C. Beroza, 2023a. En-echelon faults reactivated by
814 wastewater disposal near Musreau Lake, Alberta: *Geophysical Journal International* 235, 417-429.

815 Schultz, R., J.-U. Woo, K. Pepin, W.L. Ellsworth, H. Zebkar, P. Segall, Y.J. Gu, S. Samsonov, 2023b. Disposal from in situ
816 bitumen recovery induced the M_L 5.6 Peace River earthquake: *Geophysical Research Letters* 50, e2023GL102940.

817 Shapiro, S.A., C. Dinske, C. Langenbruch, F. Wenzel, 2010. Seismogenic index and magnitude probability of earthquakes
818 induced during reservoir fluid stimulations: *The Leading Edge* 29, 304-308.

819 Skoumal, R.J., R. Ries, M.R. Brudzinski, A.J. Barbour, B.S. Currie, 2018. Earthquakes induced by hydraulic fracturing are
820 pervasive in Oklahoma: *Journal of Geophysical Research* 123, 10918-10935.

821 Skoumal, R.J., A.J. Barbour, M.R. Brudzinski, T. Langenkamp, J.O. Kaven, 2020. Induced seismicity in the Delaware Basin,
822 Texas: *Journal of Geophysical Research* 125, e2019JB018558.

823 Skoumal, R.J., J.O. Kaven, A.J. Barbour, C. Wicks, M.R. Brudzinski, E.S. Cochran, J.L. Rubinstein, 2021. The induced M_w
824 5.0 March 2020 West Texas seismic sequence: *Journal of Geophysical Research* 126, e2020JB020693.

825 van der Elst, N.J., M.T. Page, D.A. Weiser, T.H.W. Goebel, S.M. Hosseini, 2016. Induced earthquake magnitudes are as
826 large as (statistically) expected: *Journal of Geophysical Research* 121, 4575-4590.

827 Verdon, J.P., 2016. Using microseismic data recorded at the Weyburn CCS-EOR site to assess the likelihood of induced
828 seismic activity: *International Journal of Greenhouse Gas Control* 54, 421-428.

829 Verdon, J.P. and J. Budge, 2018. Examining the capability of statistical models to mitigate induced seismicity during
830 hydraulic fracturing of shale gas reservoirs: *Bulletin of the Seismological Society of America* 108, 690-701.

831 Verdon, J.P. and J.J. Bommer, 2021. Green, yellow, red, or out of the blue? An assessment of Traffic Light Schemes to
832 mitigate the impact of hydraulic fracturing-induced seismicity: *Journal of Seismology* 25, 301-326.

833 Verdon, J.P. and G. Rodríguez-Pradilla, 2023. Assessing the variability in hydraulic fracturing-induced seismicity occurrence
834 between North American shale plays: *Tectonophysics* 859, 229898.

835 Verdon, J.P., A.L. Stork, R.C. Bissell, C.E. Bond, M.J. Werner, 2015. Simulation of seismic events induced by CO_2 injection
836 at In Salah, Algeria: *Earth and Planetary Science Letters* 426, 118-129.

837 Verdon, J.P., J-M. Kendall, A. Butcher, R. Luckett, B.J. Baptie, 2018. Seismicity induced by longwall coal mining at the
838 Thoresby Colliery, Nottinghamshire, U.K.: *Geophysical Journal International* 212, 942-954.

839 Verdon, J.P., B. Pullen, G. Rodríguez-Pradilla, 2024. Growth and stabilization of induced seismicity rates during long-term,
840 low pressure fluid injection: *Proceedings of the Royal Society Transactions A, in press*. DOI: 10.1098/rsta.2023-0183.

841 Wang, Z., X. Lei, S. Ma, X. Wang, Y. Wan, 2020. Induced earthquakes before and after cessation of long-term injections in
842 Rongchang gas field: *Geophysical Research Letters* 47, e2020GL089569.

843 Watkins, T.J.M., J.P. Verdon, G. Rodríguez-Pradilla, 2023. The temporal evolution of induced seismicity sequences
844 generated by long-term, low pressure fluid injection: *Journal of Seismology* 27, 243-259.

845 Weingarten, M., S. Ge, J.W. Godt, B.A. Bekins, J.L. Rubinstein, 2015. High-rate injection is associated with the increase in
846 U.S. mid-continent seismicity: *Science* 348, 1336-1340.

847 Yeck, W.L., A.F. Sheehan, H.M. Benz, M. Weingarten, J. Nakai, 2016. Rapid response, monitoring and mitigation of induced
848 seismicity near Greeley, Colorado: *Seismological Research Letters* 87, 837-847.

849 Yeck, W.L., G.P. Hayes, D.E. McNamara, J.L. Rubinstein, W.D. Barnhart, P.S. Earle, H.M. Benz, 2017. Oklahoma
850 experiences largest earthquake during ongoing regional wastewater injection hazard mitigation efforts: *Geophysical
851 Research Letters* 44, 711-717.

852 Zhu, W., and G.C. Beroza, 2019. PhaseNet: a deep-neural-network-based seismic arrival-time picking method: *Geophysical
853 Journal International* 216, 261-273.

854 Zöller, G. and M. Holschneider, 2016. The maximum possible and the maximum expected earthquake magnitude for
855 production-induced earthquakes at the gas field in Groningen, the Netherlands: *Bulletin of the Seismological Society
856 of America* 106, 2917-2921.

857